Stereo-hindrance Engineering of a Cation toward andlt-110andgt–oriented 2D Perovskite with Minimized Tilting and High-performance X-ray Detection

Mengling Xia, Xijuan Sun, Fan Ye, Mingquan Liao, Jiaqi Liu, S Liu, Dong Wu, Yinsheng Xu, Xianghua Zhang, Kan-Hao Xue, et al.

Stereo-hindrance Engineering of A Cation toward <110>-oriented 2D Perovskite with Minimized Tilting and High-performance X-ray Detection

Mengling Xia*, Xijuan Sun, Fan Ye, Mingquan Liao, Jiaqi Liu, Shiyou Liu, Dong Wu, Yinsheng Xu, Xianghua Zhang, Kan-Hao Xue*, Xiangshui Miao, Jiang Tang, Guangda Niu*

Prof. M. Xia, X. Sun, M. Liao, J. Liu, Dr. D. Wu, Prof. Y. Xu, Prof. X. Zhang

School of Materials Science and Engineering & State Key Laboratory of Silicate Materials for Architectures, Wuhan University of Technology, Wuhan 430070, China

E-mail: xiamengling@whut.edu.cn (M. Xia)

F. Ye, S. Liu, Prof. K. Xue, Prof. J. Tang, Prof. G. Niu

Wuhan National Laboratory for Optoelectronics (WNLO), Huazhong University of Science and Technology (HUST), Wuhan 430074, China

E-mail: guangda_niu@hust.edu.cn (G. Niu)

Prof. K. Xue, Prof. X. Miao

School of Integrated Circuits, Huazhong University of Science and Technology (HUST), Wuhan 430074, China

E-mail: xkh@hust.edu.cn (K. Xue)

This article has been accepted for publication and undergone full peer review but has not been through the copyediting, typesetting, pagination and proofreading process, which may lead to differences between this version and the Version of Record. Please cite this article as doi: 10.1002/adma.202313663.

Prof. X. Zhang

Laboratoire des Verres et Céramiques, UMR-CNRS 6226, Sciences chimiques de Rennes, Université de Rennes 1, Rennes 35042, France

Abstract

Two-dimensional <100>-oriented Dion-Jacobson or Ruddlesden-Popper perovskites have been widely recognized as promising candidates for optoelectronic applications. However, the large interlayer spacing significantly hinders the carrier transport. <110>-oriented 2D perovskites naturally exhibit reduced interlayer spacings, but the tilting of metal halide octahedra is typically serious and leads to poor charge transport. Herein, a <110>-oriented 2D perovskite $EPZPbBr_4$ (EPZ=1-ethylpiperazine) with minimized tilting is designed through A-site stereo-hindrance engineering. The piperazine functional group enters the space enclosed by the three $[PbBr_6]^{4-}$ octahedra, pushing Pb-Br-Pb closer to a straight line (maximum Pb-Br-Pb angle ~180°), suppressing the tilting as well as electron-phonon coupling. Meanwhile, the ethyl group is located between layers and contributes an extremely reduced effective interlayer distance (2.22 Å), further facilitating the carrier transport. As a result, $EPZPbBr_4$ simultaneously demonstrates high $\mu\tau$ product (1.8×10^{-3} cm^2 V^{-1}) and large resistivity (2.17×10^{10} Ω cm). The assembled X-ray detector achieves low dark current of 1.02×10^{-10} A cm^{-2} and high sensitivity of 1240 μC Gy^{-1} cm^{-2} under the same bias voltage. The realized specific detectivity (ratio of sensitivity to noise current density, 1.23×10^{8} μC Gy^{-1} cm^{-1} $A^{-1/2}$) is the highest among all reported perovskite X-ray detectors.

1. Introduction

Two-dimensional (2D) perovskites have been widely recognized as promising candidates for photoelectric applications, such as solar cell,

photodetection, LED and laser, due to their tremendous structural versatility and good moisture stability.[1-4] Present researches predominantly focus on 2D perovskites oriented along the <100> direction, described using the general formula A_2BX_4 (Ruddlesden-Popper type, RP for short, where A denotes a monovalent organic cation) or AMX_4 (Dion-Jacobson type, DJ for short, where A denotes a divalent organic cation).[5, 6] However, the wide quantum barrier significantly impacts the carrier transport, and the device performance still lags far behind 3D perovskites.[7-9] Efforts have been made to reduce the distance of the interlayer spacing of RP or DJ perovskites to facilitate the interlayer carrier transport, but it remains difficult to achieve an interlayer distance below 3 Å due to their intrinsic structure.[10, 11] The normally overlooked <110>-oriented 2D perovskite has been assembled with wavelike mutual insertion of organic and inorganic layers **(Figure 1a)**.[12] The overlapping arrangement of stacked layers naturally reduces the interlayer spacing. Unfortunately, the tilting of metal halide octahedra in <110>-oriented 2D perovskites is typically serious and inevitably deteriorates the charge transport, and the underlying mechanism of the tilting is still unclear.

Moreover, lead halide perovskites have demonstrated excellent potential for highly sensitive X-ray detection due to their high X-ray attenuation coefficients, low trap density and large mobility-lifetime product.[13-15] 3D perovskites have exhibited high sensitivity of >30000 $\mu C\ Gy^{-1}\ cm^{-2}$, which is orders of magnitude higher than commercial detectors.[16-18] The detection limit has also been decreased to below 10 $nGy\ s^{-1}$ for 2D perovskites, which is already 3 orders lower than the typical dose rate in medical imaging.[19, 20] Nevertheless, high sensitivity and low detection limit somehow contradict with each other in a single material. For example, 3D perovskites suffer from high dark current and high detection limit, while 2D perovskites exhibit poor charge transport and low sensitivity.[21, 22] Above mentioned <110>-oriented 2D perovskites could, in principle, break the trade-off between sensitivity and detection limit due to their intrinsically short interlayer distance.[23] In reality, however, very rare

successful case has been observed. It is thus significant but highly challenging to explore more <110>-oriented 2D perovskites with minimized tilting effect, to boost the practical detection performance of perovskite X-ray detectors.

Herein, we identify a <110>-oriented 2D perovskite $EPZPbBr_4$ (EPZ=1-ethylpiperazine) with minimal tilting through A-site stereo-hindrance engineering. The piperazine functional group is effective in regulating the Pb-Br-Pb bond angles close to a straight line. The high Pb-Br-Pb angle for $EPZPbBr_4$ reflects the smallest tilting of the inorganic framework as well as enhanced lattice rigidity, and consequently the suppressed electron-phonon coupling. Meanwhile, the ethyl group is located between layers and contributes an extremely reduced effective interlayer distance (2.22 Å), which is much smaller than the <100>-oriented 2D RP or DJ perovskites, further facilitating the carrier transport. As a result, high $\mu\tau$ product (1.8×10^{-3} cm^2 V^{-1}) and large resistivity (2.17×10^{10} Ω cm) are simultaneously achieved in $EPZPbBr_4$. The assembled X-ray detector exhibits a low dark current of 1.02×10^{-10} A cm^{-2} and a high sensitivity of 1240 μC Gy^{-1} cm^{-2} under the same bias voltage. The realized specific detectivity (ratio of sensitivity to noise current density, 1.23×10^{8} μC Gy^{-1} cm^{-1} $A^{-1/2}$) is the highest among all reported perovskite X-ray detectors. The proposed materials can be generally used in the fields of photoelectric detection, solar cells, electroluminescence, and so forth.

2. Result and discussion

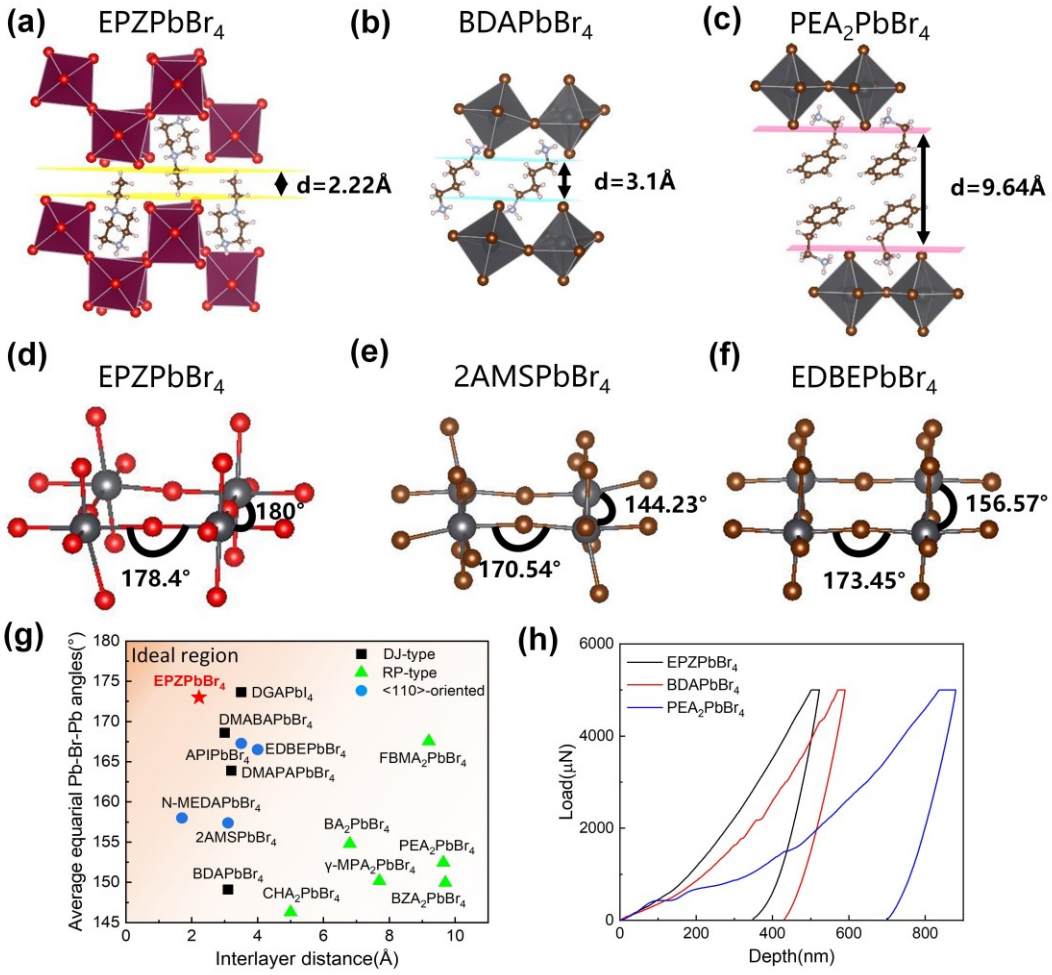

Figure 1 (a) The crystal structures of $EPZPbBr_4$. The interval between the two yellow lines is the interlayer distance. Crystal structures of (b) $BDAPbBr_4$ and (c) PEA_2PbBr_4. Pb-Br-Pb bond angles of (d) $EPZPbBr_4$, (e) $2AMSPbBr_4$ and (f) $EDBEPbBr_4$. (g) Average equatorial Pb-Br-Pb angles and interlayer distances of typical 2D perovskites. (h) Load-force-dependent indentation depth curves of $EPZPbBr_4$, $BDAPbBr_4$ and PEA_2PbBr_4 single crystals.

To illustrate the origin of specific crystal structures, the interlayer spacing and octahedral tilting of <110>-oriented 2D perovskite were investigated, along with other typical 2D perovskites for comparison. With the same formula of DJ 2D perovskite, the <110>-oriented $EPZPbBr_4$ perovskite possesses single organic layer between two adjacent inorganic

layers. The N-H···Br hydrogen bond between organic cation and [$PbBr_6$] octahedron makes it more rigid than that of RP 2D perovskite with van der Waals gap. Moreover, in the <110>-oriented structure, due to the stronger N-H···Br hydrogen bond, inorganic layer pulls the organic layer closer, forming a wavy overlapping stacking structure and thus minimizing the equivalent interlayer distance. **Figure 1a-c** depict the comparison of interlayer distance between <110>-oriented 2D perovskite, RP-2D perovskite, and DJ-2D perovskite. The widely studied PEA_2PbBr_4 RP perovskite and $BDAPbBr_4$ DJ perovskite was chose as typical ones for comparison with <110>-oriented $EPZPbBr_4$ perovskite. The interchain Br-Br distance of <110>-oriented $EPZPbBr_4$ perovskite is 2.22 Å, which is merely a fifth that of the well-known PEA_2PbBr_4 RP 2D perovskite (9.64 Å), and even shorter than the emerging $BDAPbBr_4$ (3.1 Å) and $DGAPbI_4$ (3.5 Å)[24] DJ 2D perovskites. The small interlayer spacing is beneficial for carrier transport.

Tilting of [$PbBr_6$] octahedra is another vital factor that affects the carrier transport property due to electron-phonon coupling. Tilting refers to the deviation of the metal-halide-metal angle from 180° between adjacent octahedra. For <110>-oriented 2D perovskites, organic A-site always insert into the octahedra-enclosed "half-pocket" cavity. Consequently, the volume occupied by the organic ligands within the "half-pocket" cavity is crucial for maintaining undistorted octahedral geometry (i.e., Pb-Br-Pb bond angles close to a straight line) (Table S1). **Figure 1d-f** present the comparison of the structural tilting of <110>-oriented 2D perovskites. Similar to $EPZPbBr_4$, both $2AMSPbBr_4$ (2AMS= 2-(aminoethyl)isothiourea) and $EDBEPbBr_4$ (2,2'-(ethylenedioxy)bis(ethylammonium)) also belong to the typical <110>-oriented perovskites (**Table S2**, **S3** and **S4**). 2AMS and EDBE are both chain organic ligands, while EPZ assembles with a piperazine ring (Figure S1). Through A-site stereo-hindrance engineering, the piperazine functional group (79.8 $Å^3$) is filled in the space (129.3 Å) enclosed by the three $[PbBr_6]^{4-}$ octahedra to achieve a spatial fit (Table S1), pushing Pb-Br-Pb closer to a straight line (maximum Pb-Br-Pb angle ~180°). As shown in **Figure 1g**, the minimum tilting $EPZPbBr_4$ with a high average Pb-Br-Pb angle

was much more superior to other <110>-oriented perovskites. The stereo-hindrance engineering also guarantees that the penetration depth of NH_3 in the inorganic layer is only 1.0 Å (Figure S2), smaller than that reported previously for the DJ-type perovskite $DGAPbI_4$ (1.2 Å)[24] and also smaller than all other <110>-oriented perovskites currently known.[25, 26] The binding energy of both Pb 4f and Br 3d of $EPZPbBr_4$ were higher than that of $2AMSPbBr_4$ and $EDBEPbBr_4$ (Figure S3), indicating the decreased electron cloud density due to stronger hydrogen bond.

To further validate the stereo-hindrance engineering of EPZ molecules, we performed first-principles simulations to add $-CH_3$ groups on piperazine ring or reduce the $-CH_2-$ group of piperazine ring of EPZ molecules in order to modify the stereo-hindrance. The results indicate that regardless of whether the $-CH_3$ groups are added or reduced, the resulting octahedral structures exhibit pronounced tilting (Figure S4). This finding further corroborates our previous hypothesis regarding the impact of the volume occupied by organic ligands, i.e. stereo-hindrance effect, on octahedral tilting. It also demonstrates that EPZ organic ligand offers the most effective stereo-hindrance, resulting in the suppressed octahedral tilting in <110>-oriented 2D perovskites. The smallest tilting facilitates the carrier transport through suppressed electron-phonon coupling.

We prepared high-quality $EPZPbBr_4$ single crystals with the transmittance exceeding 85% through a slow cooling crystallization method (Figure S5). $BDAPbBr_4$ and PEA_2PbBr_4 single crystals were also synthesized according to a solvent evaporation method.[27] The fresh surfaces of the three kinds of single crystals were measured by nanoindentation experiments to reflect the crystal rigidity. Under a 5000 μN load, the load-displacement depth curves corresponding to $EPZPbBr_4$, $BDAPbBr_4$, and PEA_2PbBr_4 are shown in **Figure 1h**, reflecting the elastic and plastic deformations occurring near the nanotip. Smaller indentation depths of $EPZPbBr_4$, compared with $BDAPbBr_4$ and PEA_2PbBr_4, corresponded to less elastic deformation and hence greater hardness.[28] Also, $EPZPbBr_4$ possesses a higher Young's modulus (16.65 GPa) than $BDAPbBr_4$ (15.89 GPa) and PEA_2PbBr_4 (9.73 GPa) (Figure S6), indicating a superior resistance to elastic deformation

and thus a stronger crystal rigidity, which yields weaker electron-phonon coupling. To verify this point, temperature-dependent PL spectra of $EPZPbBr_4$ were obtained, as shown in Figure S7. The deformation potential (D), which is the shift in energy band per unit strain, has been widely used to quantity the intensity of electron-phonon coupling since 1950.[29] Procedure on the calculation of D based on the FWHM broadening of PL spectra is illustrated in Figure S8 and discussed in Supplementary Note I. The electron-phonon coupling strength of $EPZPbBr_4$ is lower than that of $BDAPbBr_4$. It turns out that the diminished tilting can effectively suppress electron-phonon coupling through enhancing the rigidity of the <110>-oriented crystal.

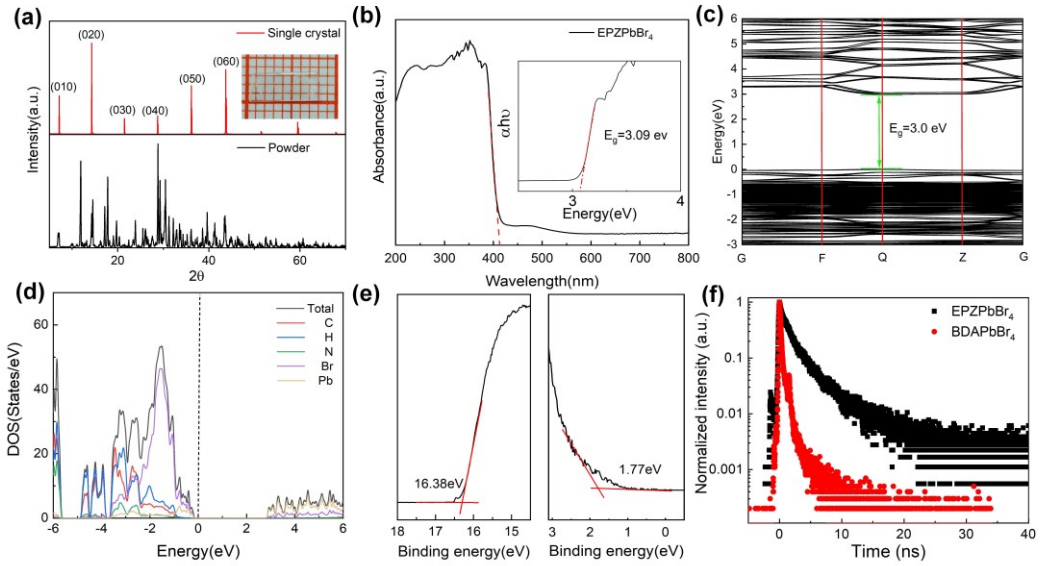

Figure 2 (a) Crystal and powder XRD patterns of $EPZPbBr_4$, where the inset is a photograph of $EPZPbBr_4$ single crystal. (b) Absorption spectrum of $EPZPbBr_4$. The inset shows the corresponding Tauc plot. (c) Calculated electronic band structure of $EPZPbBr_4$ from density functional theory simulation. (d) Total and partial densities of states (DOS) spectra of $EPZPbBr_4$ through calculation. (e) UV photoelectron spectroscopy of $EPZPbBr_4$. (f) Time-resolved PL spectra of $EPZPbBr_4$ and $BDAPbBr_4$ single crystals.

The synthesized $EPZPbBr_4$ single crystal was colorless with regular shape, reaching an impressive size of ~8 mm×3 mm×0.5 mm (**Figure 2a**). The X-ray diffraction (XRD) pattern of $EPZPbBr_4$ single crystal show good orientation. The exposed natural cleavage plane tends to be defined as the {001} group of crystallographic planes by single crystal structure measurement to obtain cell parameters conveniently. It should be noted that the (010), (020), (030)… planes marked in the XRD pattern (**Figure 2a**) is the planes cut out from 3D structure along <110> direction (Figure S2). From the powder XRD pattern and single crystal structural analysis, the crystal space group was identified as *P*2/*c*, with cell parameters: a=10.5477 Å, b=12.4246 Å, c=16.4302(1) Å, α=90°, β=96.733°, γ=90° (see Table S2 for detailed crystal structure parameters). From the UV-Vis spectra of $EPZPbBr_4$ single crystal (**Figure 2b**), the direct band gap was verified and calculated to be 3.09 eV by the Tauc curve. The band structure was further investigated by first-principles calculations, using a self-energy corrected shell DFT-1/2 method.[30-32] The valence band maximum (VBM) and conduction band minimum (CBM) of $EPZPbBr_4$ are both located at the Q-point with the theoretical $EPZPbBr_4$ bandgap of 3.0 eV, consistent with the experimental results (**Figure 2c**). The corresponding projected density of states (PDOS) shows that the VBM is mainly derived from Br p states, with a small contribution from Pb s state, while the CBM stems from the hybridized Pb p and Br p states (**Figure 2d**). To determine the energy levels of $EPZPbBr_4$, ultraviolet photoelectron spectroscopy (UPS) was performed, with results shown in **Figure 2e**. The value of work function and valence band edge can be obtained from the tangent of the cutoff edge. Based on the absorption spectrum and UPS spectrum, the energy level diagram indicates that the CBM, VBM, and Fermi level are located at -3.52 eV, -6.61 eV, and -4.84 eV (Figure S9), respectively, revealing an n-type doping. Notably, the average carrier lifetime of $EPZPbBr_4$ is longer than that of $BDAPbBr_4$, as shown in **Figure 2f**. The fast and slow components of decay time are usually assigned to the non-radiation recombination of carriers by the surface defects and recombination in the bulk, respectively.

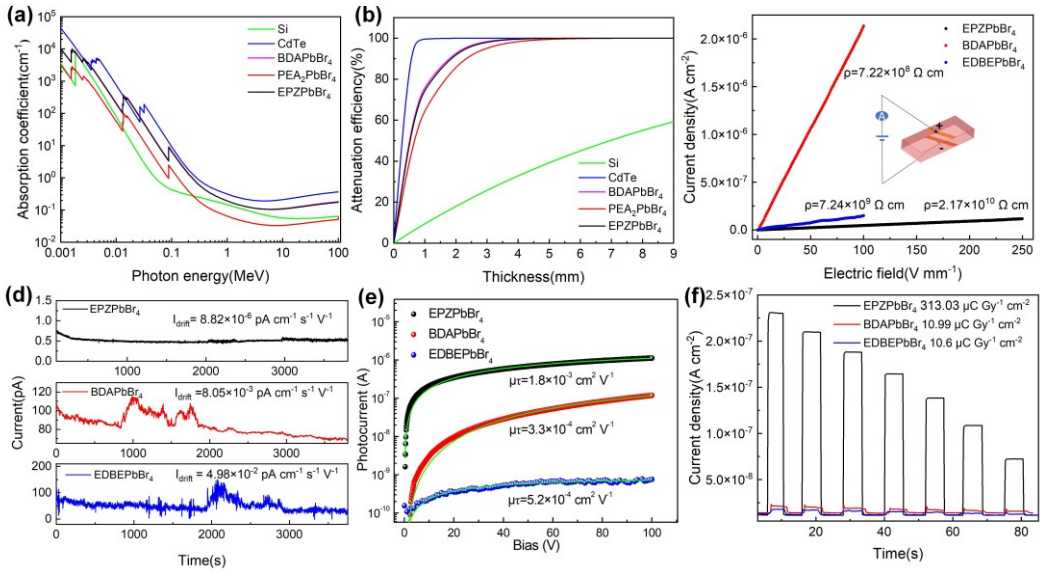

Figure 3 (a) Absorption coefficient of a few representative semiconductors as a function of photon energy. (b) Attenuation efficiency against 50 keV X-ray photons of a few representative semiconductors as a function of thickness. (c) I-V curves of $EPZPbBr_4$, $BDAPbBr_4$ and $EDBEPbBr_4$ single crystals. The inset is the device structure for I-V curve testing. (d) Dark current drift of $EPZPbBr_4$, $BDAPbBr_4$ and $EDBEPbBr_4$ single crystal devices. (e) Voltage-dependent photoconductivity of $EPZPbBr_4$ and $EDBEPbBr_4$ device. (f) I-T curves of $EPZPbBr_4$, $BDAPbBr_4$ and $EDBEPbBr_4$ under different X-ray dose rates from 580 to 82.86 μGy s^{-1}.

ctor

should have large average atomic number and high mass density to ensure the sufficient absorption of X-ray photons. The average atomic number of $EPZPbBr_4$ at 50 keV (which is the intensity climax of our X-ray source) is 26.77, higher than PEA_2PbBr_4 (25.54) and $BDAPbBr_4$ (21.56). The effective atomic number was calculated by the established software "AutoZeff".[33] As shown in **Figure 3a**, the X-ray absorption coefficients of $EPZPbBr_4$, PEA_2PbBr_4, $BDAPbBr_4$, CdTe and Si at photon energies from 1 keV to 1 MeV were calculated using the XCOM Photon Cross Sections Database. The absorption coefficient of $EPZPbBr_4$ is comparable to BDA_2PbBr_4 2D DJ perovskite and much superior than PEA_2PbBr_4 2D RP perovskite withing the whole photon energy

range. The attenuation efficiency was depicted versus thickness curves of above semiconductors toward 50 keV X-rays. A thickness of 1.2 mm is enough to attenuate 80% of 50 keV X-rays, shorter than the well-known PEA_2PbBr_4 (1.6 mm).

Carrier transport is another key factor influencing X-ray detection performance. Principally, to achieve complete charge collection, the thickness of the detector should be smaller than the Schubweg value $\mu\tau E$, where μ is the carrier mobility, τ is the carrier lifetime, and E is the external bias field. The Schubweg value is the distance across which the carrier can be transported for a given electric field before annihilation. Utilizing the modified Hecht equation $I = \frac{I_0 \mu\tau U}{\mathrm{d}^2}\left(1-\exp\left(-\frac{\mathrm{d}^2}{\mu\tau U}\right)\right)$ (I_0 is the saturated photocurrent, d is the crystal thickness, and U is the applied bias)[34-36], the carrier mobility lifetime product ($\mu\tau$) of $EPZPbBr_4$ was obtained as $1.8(\pm0.02)\times10^{-3}$ cm^2 V^{-1} (**Figure 3e**). This value is much higher than that of $BDAPbBr_4$ ($3.3(\pm0.03)\times10^{-4}$ cm^2 V^{-1}) and other <110>-oriented perovskite $EDBEPbBr_4$ ($5.2(\pm0.1)\times10^{-4}$ cm^2 V^{-1}).

Previous study demonstrated that the Schottky contact between metal and perovskite is beneficial for reducing the dark current in a photodetector. Ag metal was selected as the electrodes and an Ag/$BDAPbBr_4$/Ag device of vertical structure was fabricated (**Figure 3c**). The resistivity at forward bias was 2.17×10^{10} Ω cm for $EPZPbBr_4$, larger than 7.22×10^{8} Ω cm for $BDAPbBr_4$ (**Figure 3c**) and 7.24×10^{9} Ω cm for $EDBEPbBr_4$, indicating higher barrier at contact as well as within the bulk crystals. High resistivity is conducive to reducing the dark current of the device, thus increasing the operation stability and facilitating the integration with the back-end circuit.

The dark current drift was measured at a bias of 10 V for 1 h. The calculated baseline drift of $EPZPbBr_4$ is 8.82×10^{-6} pA cm^{-1} s^{-1} V^{-1} (**Figure 3d**), which is much smaller than that of $BDAPbBr_4$ (8.05×10^{-3} pA cm^{-1} s^{-1} V^{-1}) and $EDBEPbBr_4$ (4.98×10^{-2} pA cm^{-1} s^{-1} V^{-1}) according to $I_{\mathrm{drift}} = (I_{\mathrm{t}}\text{-}I_0)/tsE$, where

I_t and I_0 are the starting current and the ending current, respectively, t is the interval time, and s is the electrode area. Besides, the fluctuation standard variances of $EPZPbBr_4$, $BDAPbBr_4$ and $EDBEPbBr_4$ devices were 0.04, 10.89 and 18.6 pA, respectively. Both the dark current drift and the fluctuation of the $EPZPbBr_4$ device imply a better stability than $BDAPbBr_4$ and $EDBEPbBr_4$, due to the much higher resistivity of $EPZPbBr_4$. Based on the large resistivity and high $\mu\tau$ product, the $EPZPbBr_4$ device exhibits a good X-ray response, with response magnitude and stability far superior to that of $BDAPbBr_4$ and $EDBEPbBr_4$ (**Figure 3f**). Besides, the response of 2D PEA_2PbBr_4 RP perovskite to X-rays was also worse than that of 2D $EPZPbBr_4$ <110>-oriented perovskite due to the large interchain Br-Br distance and poor carrier transport (Figure S10).

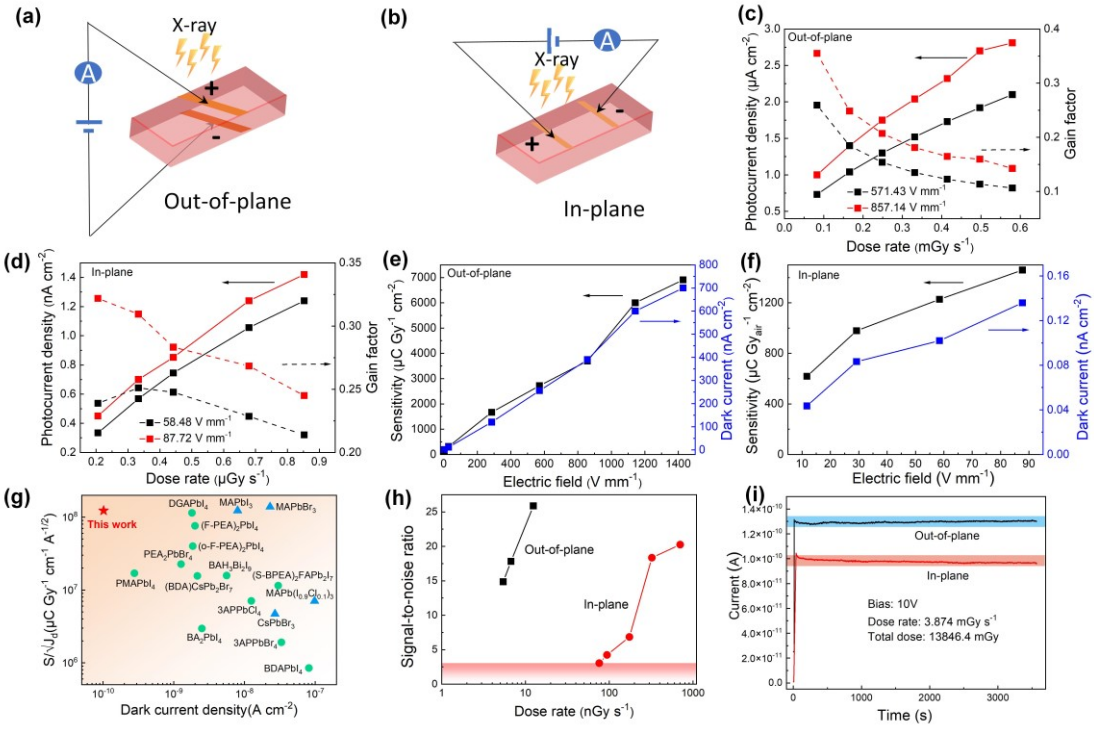

Figure 4 Illustration of the X-ray detector with (a) out-of-plane structure and (b) in-plane structure exposing to X-rays. X-ray photocurrent density and gain factor as a function of X-ray dose rate of (c) out-of-plane structure and (d) in-plane structure. Solid lines represent photocurrent density and dashed lines represent gain factor. Calculated sensitivity as a

function of electric field of (e) out-of-plane structure and (f) planar structure. (g) Summary of the reported dark current and the ratio of sensitivity to noise current for X-ray detectors. (h) Signal-to-noise ratio (SNR) of the devices. The top edge of the filled region represents an SNR of 3. (i) Photocurrent stability of $EPZPbBr_4$ detector exposed to X-rays (3.874 mGy s^{-1}) for 1 h.

To investigate the X-ray detection performance of $EPZPbBr_4$ perovskites, photoconductive devices with both planar and vertical structures were fabricated, respectively (**Figure 4a** and **4b**). The devices were exposed to a tungsten anode X-ray tube with the photon energy up to 50 keV. The radiation dose rate was modulated by changing the current of the X-ray tube or the distance between the X-ray source and the device. The dose rate was carefully calibrated by a Radcal ion chamber dosimeter. The generated photocurrent by X-ray irritation as well as the gain factor of the out-of-plane and in-plane directions are shown in **Figure 4c** and **4d**, respectively. With the increased dose rate, the photocurrent increased linearly, which is a common phenomenon in photodetectors. The photoconductive gain is generated by the filling of charge carriers into the shallow trap of the single crystals. As the photoexcited electrons can be easily trapped by the shallow defects, the photoexcited holes traverse between the electrodes multiple times during this trapping period.[37] The gain factors under various dose rates can be calculated accordingly (see Supporting Information Note II). The gain gradually decreased upon increasing the dose rate, which is known as the dynamic-range enhancing gain compression. The calculated gain factor of $EPZPbBr_4$ single crystal detector in out-of-plane direction was 0.18-0.35 for the dose rates of 82.3-331.4 μGy s^{-1}, higher than that of $Rb_3Bi_2I_9$ X-ray detector (0.172-0.194 at 87.46-204.08 μGy s^{-1}), $MAPbBr_3$ X-ray detectors (0.164 at 0.86 μGy s^{-1}) and $Cs_2AgBiBr_6$ single crystal X-ray detectors (0.14 at 60-138.7 μGy s^{-1}).[19, 34, 37] For in-plane direction, the gain factor of $EPZPbBr_4$ single crystal detector was > 0.2, even at a low dose rate. The high gain factor brings large photocurrent and thus high sensitivity, overcoming the limit of high ionization energy caused by the wide bandgap.

dose rate of 3.874 mGy s^{-1} under 10 V bias for 1 h (**Figure 4i**). The photocurrent of $EPZPbBr_4$ detector remains stable after irradiation with the accumulated dose of 1.38 Gy, while the photocurrent of $BDAPbBr_4$ detector dropped to 52.6% of the initial value under the same condition (Figure S11). Also, the standard deviation of $EPZPbBr_4$ detector (1.0×10^{-12}) is smaller than $BDAPbBr_4$ detector (1.29×10^{-11}) and 1,000 times smaller than the typical 3D $MAPbBr_3$ detector (Figure S12). The X-ray on-off test further demonstrated the high operating stability of $EPZPbBr_4$ device for X-ray detection (Figure S13).

3. Conclusion

In summary, we report a novel strategy of stereo-hindrance engineering of A-site in <110>-oriented 2D perovskites, in order to effectively minimize the tilting in the inorganic framework. The introduced piperazine functional group helps to push the Pb-Br-Pb bonds closer to a straight line (maximum Pb-Br-Pb angle ~180°), rendering suppressed octahedral tilting and accordingly weaker electron-phonon coupling. Moreover, the extremely reduced effective interlayer distance (2.22 Å), which is smaller than <100>-oriented 2D perovskites, further facilitates the carrier transport. The rare combination of minimal tilting and small interlayer distance renders $EPZPbBr_4$ a promising candidate for photodetection applications. As an example, the $EPZPbBr_4$ X-ray detector achieves low dark current of 1.02×10^{-10} A cm^{-2} and high sensitivity of 1240 μC Gy^{-1} cm^{-2} under the same bias voltage. The realized specific detectivity (ratio of sensitivity to noise current density, 1.23×10^{8} μC Gy^{-1} cm^{-1} $A^{-1/2}$) is the highest among all reported perovskite X-ray detectors. This work provides a stereo-hindrance engineering insight to minimize tilting of 2D <110>-oriented perovskites, which is also beneficial for other perovskite optoelectronic devices such as light emitting diodes, lasers and photodetectors.

Acknowledgement

This work was financially supported by the National Natural Science Foundation of China (U2330115, 62275206, U2241236). The authors thank the Analytical and Testing Center of HUST and the facility support of the Center for Nanoscale Characterization and Devices (CNCD), WNLO-HUST.

Reference

[1] H. Tsai, W. Nie, J.-C. Blancon, C. C. Stoumpos, R. Asadpour, B. Harutyunyan, A. J. Neukirch, R. Verduzco, J. J. Crochet, S. Tretiak, L. Pedesseau, J. Even, M. A. Alam, G. Gupta, J. Lou, P. M. Ajayan, M. J. Bedzyk, M. G. Kanatzidis, A. D. Mohite, *Nature* **2016**, 536, 312-316.

[2] F. Zhang, S. Y. Park, C. Yao, H. Lu, S. P. Dunfield, C. Xiao, S. Uličná, X. Zhao, L. Du Hill, X. Chen, X. Wang, L. E. Mundt, K. H. Stone, L. T. Schelhas, G. Teeter, S. Parkin, E. L. Ratcliff, Y.-L. Loo, J. J. Berry, M. C. Beard, Y. Yan, B. W. Larson, K. Zhu, *Science* **2022**, 375, 71-76.

[3] Z. Chu, Y. Zhao, F. Ma, C.-X. Zhang, H. Deng, F. Gao, Q. Ye, J. Meng, Z. Yin, X. Zhang, J. You, *Nat. Commun.* **2020**, 11, 4165.

[4] T. Jin, Z. Liu, J. Luo, J.-H. Yuan, H. Wang, Z. Xie, W. Pan, H. Wu, K.-H. Xue, L. Liu, Z. Hu, Z. Zheng, J. Tang, G. Niu, *Nat. Commun.* **2023**, 14, 2808.

[5] L. Mao, W. Ke, L. Pedesseau, Y. Wu, C. Katan, J. Even, M. R. Wasielewski, C. C. Stoumpos, M. G. Kanatzidis, *J. Am. Chem. Soc.* **2018**, 140, 3775-3783.

[6] P. Huang, S. Kazim, M. Wang, S. Ahmad, *ACS Energy Lett.* **2019**, 4, 2960-2974.

[7] X. Li, J. M. Hoffman, M. G. Kanatzidis, *Chem. Rev.* **2021**, 121, 2230-2291.

[8] Y. Zhao, H. Xiang, R. Ran, W. Zhou, W. Wang, Z. Shao, *J. Energy Chem.* **2023**, 83, 189-208.

[9] L. Liu, J. Lu, H. Wang, Z. Cui, G. Giorgi, Y. Bai, Q. Chen, *Materials Reports: Energy* **2021**, 1, 100064

[10] C. Liu, Z. Fang, J. Sun, Q. Lou, J. Ge, X. Chen, E. Zhou, M.-H. Shang, W. Yang, Z. Ge, *ACS Energy Lett.* **2020**, 5, 3617-3627.

[11] S. Yu, Y. Yan, M. Abdellah, T. Pullerits, K. Zheng, Z. Liang, *Small* **2019**, 15, 1905081.

[12] C. Qin, L. Xu, Z. Zhou, J. Song, S. Ma, Z. Jiao, Y. Jiang, *J. Mater. Chem. A* **2022**, 10, 3069-3076.

[13] D. Shi, V. Adinolfi, R. Comin, M. Yuan, E. Alarousu, A. Buin, Y. Chen, S. Hoogland, A. Rothenberger, K. Katsiev, Y. Losovyj, X. Zhang, P. A. Dowben, O. F. Mohammed, E. H. Sargent, O. M. Bakr, *Science* **2015**, 347, 519-522.

[14] Q. Dong, Y. Fang, Y. Shao, P. Mulligan, J. Qiu, L. Cao, J. Huang, *Science* **2015**, 347, 967-970.

[15] H. Wei, J. Huang, *Nat. Commun.* **2019**, 10, 1066.

[16] J. Pang, S. Zhao, X. Du, H. Wu, G. Niu, J. Tang, *Light: Sci. Appl.* **2022**, 11, 105.

[17] H. Wei, D. DeSantis, W. Wei, Y. Deng, D. Guo, T. J. Savenije, L. Cao, J. Huang, *Nat. Mater.* **2017**, 16, 826-833.

[18] M. Hu, S. Jia, Y. Liu, J. Cui, Y. Zhang, H. Su, S. Cao, L. Mo, D. Chu, G. Zhao, K. Zhao, Z. Yang, S. F. Liu, *ACS Appl. Mater. Interfaces* **2020**, 12, 16592-16600.

[19] M. Xia, J.-H. Yuan, G. Niu, X. Du, L. Yin, W. Pan, J. Luo, Z. Li, H. Zhao, K.-H. Xue, X. Miao, J. Tang, *Adv. Funct. Mater.* **2020**, 30, 1910648.

[20] M. Chen, X. Dong, D. Chu, B. Jia, X. Zhang, Z. Zhao, J. Hao, Y. Zhang, J. Feng, X. Ren, Y. Liang, R. Shi, A. Najar, Y. Liu, S. Liu, *Adv. Mater.* **2023**, 35, 2211977.

[21] Y. Xiao, C. Xue, X. Wang, Y. Liu, Z. Yang, S. Liu, *ACS Appl. Mater. Interfaces* **2022**, 14, 54867-54875.

[22] H. Kanda, V. Dan Mihailetchi, M.-E. Gueunier-Farret, J.-P. Kleider, Z. Djebbour, J. Alvarez, B. Philippe, O. Isabella, M. R. Vogt, R.

Santbergen, P. Schulz, F. Peter, M. K. Nazeeruddin, J. P. Connolly, *Interdisciplinary Materials* **2022**, 1, 148-156.

[23] J. Xi, J. Byeon, U. Kim, K. Bang, G. R. Han, J.-Y. Kim, J. Yoon, H. Dong, Z. Wu, G. Divitini, K. Xi, J. Park, T.-W. Lee, S. K. Kim, M. Choi, J. W. Lee, *Energy Environ. Sci.* **2021**, 14, 4915-4925.

[24] B. Zhang, T. Zheng, J. You, C. Ma, Y. Liu, L. Zhang, J. Xi, G. Dong, M. Liu, S. Liu, *Adv. Mater.* **2023**, 35, 2208875.

[25] K.-z. Du, Q. Tu, X. Zhang, Q. Han, J. Liu, S. Zauscher, D. B. Mitzi, *Inorg. Chem.* **2017**, 56, 9291-9302.

[26] Y. Mo, C. Wang, X. Zheng, P. Zhou, J. Li, X. Yu, K. Yang, X. Deng, H. Park, F. Huang, Y.-B. Cheng, *Interdisciplinary Materials* **2022**, 1, 309-315.

[27] Y. Gao, P. Wan, T. Jin, H. Hu, L. Liu, G. Niu, *Sma//* **2023**, 19, 2301530.

[28] M. A. Reyes-Martinez, A. L. Abdelhady, M. I. Saidaminov, D. Y. Chung, O. M. Bakr, M. G. Kanatzidis, W. O. Soboyejo, Y.-L. Loo, *Adv. Mater.* **2017**, 29, 1606556.

[29] A. Franceschetti, S.-H. Wei, A. Zunger, *Phys. Rev. B* **1994**, 50, 17797-17801.

[30] K.-H. Xue, J.-H. Yuan, L. R. C. Fonseca, X.-S. Miao, *Comput. Mater. Sci.* **2018**, 153, 493-505.

[31] L. G. Ferreira, M. Marques, L. K. Teles, *Phys. Rev. B* **2008**, 78, 125116.

[32] G.-Q. Mao, Z.-Y. Yan, K.-H. Xue, Z. Ai, S. Yang, H. Cui, J.-H. Yuan, T.-L. Ren, X. Miao, *J. Phys.: Condens.Matter* **2022**, 34, 403001.

[33] M. L. Taylor, R. L. Smith, F. Dossing, R. D. Franich, *Medical Physics* **2012**, 39, 1769-1778.

[34] H. Wei, Y. Fang, P. Mulligan, W. Chuirazzi, H.-H. Fang, C. Wang, B. R. Ecker, Y. Gao, M. A. Loi, L. Cao, J. Huang, *Nat. Photonics* **2016**, 10, 333-339.

[35] Y. Liu, H. Ye, Y. Zhang, K. Zhao, Z. Yang, Y. Yuan, H. Wu, G. Zhao, Z. Yang, J. Tang, Z. Xu, S. Liu, *Matter* **2019**, 1, 465-480.

[36] Y.-M. Xie, Q. Yao, Q. Xue, Z. Zeng, T. Niu, Y. Zhou, M.-P. Zhuo, S.-W. Tsang, H.-L. Yip, Y. Cao, *Interdisciplinary Materials* **2022**, 1, 281-293.

[37] W. C. Pan, H. D. Wu, J. J. Luo, Z. Deng, C. Ge, C. Chen, X. Jiang, W.-J. Yin, G. Niu, L. Zhu, L. Yin, Y. Zhou, Q. Xie, X. Ke, M. Sui, J. Tang, *Nat. Photonics* **2017**, 11, 726-732.

[38] M. L. Xia, Z. H. Song, H. D. Wu, X. Du, X. He, J. Pang, H. Luo, L. Jin, G. Li, G. Niu, J. Tang, *Adv. Funct. Mater.* **2022**, 2110729.

[39] H. Li, J. Song, W. Pan, D. Xu, W.-a. Zhu, H. Wei, B. Yang, *Adv. Mater.* **2020**, 32, 2003790.

[40] B. Zhang, Z. Xu, C. Ma, H. Li, Y. Liu, L. Gao, J. Zhang, J. You, S. Liu, *Adv. Funct. Mater.* **2022**, 32, 2110392.

[41] C. Ma, H. Li, M. Chen, Y. Liu, K. Zhao, S. Liu, *Adv. Funct. Mater.* **2022**, 32, 2202160.

[42] Y. Shen, Y. Liu, H. Ye, Y. Zheng, Q. Wei, Y. Xia, Y. Chen, K. Zhao, W. Huang, S. Liu, *Angew. Chem. Int. Ed.* **2020**, 59, 14896-14902.

[43] C. Ma, L. Gao, Z. Xu, X. Li, X. Song, Y. Liu, T. Yang, H. Li, Y. Du, G. Zhao, X. Liu, M. G. Kanatzidis, S. F. Liu, K. Zhao, *Chem. Mater.* **2022**, 34, 1699-1709.

[44] Yukta, J. Ghosh, M. A. Afroz, S. Alghamdi, P. J. Sellin, S. Satapathi, *ACS Photonics* **2022**, 9, 3529-3539.

[45] C.-X. Qian, M.-Z. Wang, S.-S. Lu, H.-J. Feng, *Appl. Phys. Lett.* **2022**, 120, 011901.

[46] Q. Guan, H. Ye, S. You, Z.-K. Zhu, H. Li, X. Liu, J. Luo, *Small* **2023**, 2307908.

[47] F. Lédée, A. Ciavatti, M. Verdi, L. Basiricò, B. Fraboni, *Adv. Opt. Mater.* **2022**, 10, 2101145.

[48] B. Xiao, Q. Sun, S. Wang, L. Ji, Y. Li, S. Xi, B.-B. Zhang, J. Wang, W. Jie, Y. Xu, *J. Phys. Chem. Lett.* **2022**, 13, 1187-1193.

[49] Q. Xu, X. Wang, H. Zhang, W. Shao, J. Nie, Y. Guo, J. Wang, X. Ouyang, *ACS Applied Electronic Materials* **2020**, 2, 879-884.

[50] W. Wei, Y. Zhang, Q. Xu, H. Wei, Y. Fang, Q. Wang, Y. Deng, T. Li, A. Gruverman, L. Cao, J. Huang, *Nature Photonics* **2017**, 11, 315-321.

[51] Y. C. Kim, K. H. Kim, D. Y. Son, D. N. Jeong, J. Y. Seo, Y. S. Choi, I. T. Han, S. Y. Lee, N. G. Park, *Nature* **2017**, 550, 87-+.

[52] J. J. Zhao, L. Zhao, Y. H. Deng, X. Xiao, Z. Ni, S. Xu, J. Huang, *Nature Photonics* **2020**, 14, 612-617.

Table of Contents

A <110>-oriented 2D $EPZPbBr_4$ (EPZ=1-ethylpiperazine) perovskite with minimized tilting and interlayer distance is designed through A-site stereo-hindrance engineering. The piperazine functional group enters the space enclosed by the three $[PbBr_6]^{4-}$ octahedra, pushing Pb-Br-Pb closer to a straight line (maximum Pb-Br-Pb angle ~180°), suppressing the tilting as well as electron-phonon coupling. The $EPZPbBr_4$ X-ray detector exhibits excellent specific detectivity (1.23×10^8 $\mu C\ Gy^{-1}\ cm^{-1}\ A^{-1/2}$).